

# The Andromeda System: A new orbital history and its implications

Thor Tepper-García,<sup>1,2</sup>★ Joss Bland-Hawthorn,<sup>1,2</sup> and Di Li<sup>3,4,5</sup>

<sup>1</sup>*Sydney Institute for Astronomy, School of Physics, University of Sydney, NSW 2006, Australia*

<sup>2</sup>*Centre of Excellence for All Sky Astrophysics in Three Dimensions (ASTRO-3D), Australia*

<sup>3</sup>*Key Laboratory of the Five-hundred-meter Aperture Spherical radio Telescope (FAST),*

*National Astronomical Observatories, Chinese Academy of Sciences, Beijing 100101, China*

<sup>4</sup>*School of Astronomy and Space Science, University of Chinese Academy of Sciences, Beijing 101408, China*

<sup>5</sup>*NAOC-UKZN Computational Astrophysics Centre, University of KwaZulu-Natal, Durban 4000, South Africa*

Accepted —. Received —; in original form —

## ABSTRACT

We revisit the orbital history of the Triangulum galaxy (M33) around the Andromeda galaxy (M31) in view of the recent *Gaia* Data Release 2 proper motion measurements for both Local Group galaxies. Earlier studies consider highly idealized dynamical friction, but neglect the effects of dynamical mass loss. We show the latter process to be important using orbit integrations and N-body simulations, which are mutually consistent. Contrary to previous claims that only a ‘first infall’ is supported by the data, we find an orbital solution that brings these galaxies to within  $\sim 50$  kpc of each other in the past, i.e.  $\sim 6.5$  Gyr ago. We explore the implications of this finding using a N-body/hydrodynamical simulation to model the infall of M33 into M31 with a focus on the origin of two prominent features of this system: 1) M31’s metal-rich Giant Stellar Stream; and 2) the M31-M33 H<sub>I</sub> filament. We find that the tidal interaction does not produce a stellar structure reminiscent of the stellar stream that survives up to the present day. The observed, outer disc warp in M33 may well be a relic of this past interaction. Similarly, the H<sub>I</sub> filament is likely a fossil structure dating back to the time of the ancient encounter between these galaxies. Our model implies the existence of a much larger, diffuse gas stream, the ‘Triangulum stream’, that extends from M33 away from M31. We anticipate upcoming observations with the recently commissioned, Five-hundred-meter Aperture Spherical radio Telescope (FAST) that will target the putative stream in its first years of operation.

**Key words:** Local Group, galaxies: interaction, galaxies: individual: Andromeda, galaxies: individual: Triangulum, methods: numerical

## 1 INTRODUCTION

The archaeology of the Local Group is of profound importance in modern astrophysics. Kourkchi & Tully (2017) show that the Local Group is very typical of galaxy groups in the local Universe since most are dominated by a few  $L_\star$  galaxies. There are many questions we can ask about the Local Group that are presently impossible to consider for any other group. Within a few decades, we are likely to have 6D phase space coordinates for all major Local Group galaxies, including many of the constituents like globular clusters and dwarf galaxies. This may even allow us to ‘unravel’ the orbits over billions of years to see how the Local Group has evolved dynamically.

M31 is comparable to or possibly larger than the Milky Way by mass (Diaz et al. 2014; McMillan 2017). Many recent observations serve to show key differences between both systems, due to the different accretion histories over the past 10 Gyr (Kormendy 2013; Ferguson & Mackey 2016). M31’s bulge is more dominant than the

compact bulge/bar system in the Milky Way (Courteau et al. 2011); its central supermassive black hole is also 50 times more massive than Sgr A\* (Bland-Hawthorn & Gerhard 2016). Long-running stellar surveys reveal a wealth of evidence for late major mergers throughout M31’s halo (SPLASH: Gilbert et al. 2009; PHAT: Dalcanton et al. 2012; PAndAS: Ibata et al. 2014). Notably, the PAndAS survey has spent the last decade mapping out the environments of both M31 and M33 to reveal a rich structure of faint stellar wisps and streams (McConnachie et al. 2009; Lewis et al. 2013; McConnachie et al. 2018).

The disk of M31 also shows major differences from the Milky Way: these include a very active star formation history over the past 4 Gyr (Bernard et al. 2015; Williams et al. 2015), and a thick stellar disc that dominates over the thin disc component (Dorman et al. 2015). The Milky Way’s recent history is relatively quiescent, in particular, most of the stellar mass is locked up in a thin stellar disc.

The recent surveys of M31’s environment have focussed on the stellar components with the goal to understand M31’s assembly history, but there are certain to be important clues from the gas

★ tepper@physics.usyd.edu.au

phases about its accretion history as well. The limited H<sub>I</sub> surveys to date have already revealed interesting structures, e.g. [Braun & Thilker \(2004\)](#) identified H<sub>I</sub> between M31 and M33, part of which was further resolved to discrete structures by the GBT ([Wolfe et al. 2013](#)) and some was shown to display a coherent structure ([Kerp et al. 2016](#)). Gas streams around M31 have been detected in emission (H<sub>I</sub>; e.g. [Lockman et al. 2012](#)) and in absorption (ultra-violet atomic transitions; [Koch et al. 2015](#)) extending from M31 both away from and towards M33. Similarly, the gas around M33 detected in the form of H<sub>I</sub> displays a disturbed morphology ([Putman et al. 2009](#)). We need to understand where to look near M31 and how we should target diffuse or clumpy gas. We can also look for gas associated with the stellar streams, and address open questions surrounding the known H<sub>I</sub> features. For example, is the gas bridge observed between M31 and M33 the result of an interaction ([Bekki 2008](#)) or rather the product of condensation within an intergalactic filament ([Wolfe et al. 2013, 2016](#))? What is the origin of M33's disturbed H<sub>I</sub> morphology?

New radio telescopes coming online, e.g. the Five-hundred-meter Aperture Spherical radio Telescope (FAST; [Nan et al. 2011](#); [Li & Pan 2016](#)), will soon allow us to survey M31's and M33's gas distribution more extensively and to lower column density threshold, which can survive the cosmic and galactic ionizing intensity out to 50-100 kpc in galactic radius if sufficiently clumpy ([Bland-Hawthorn et al. 2017](#)). With the FAST L-band array of 19 feed-horns (FLAN), we have realized an unprecedented commensal survey mode for searching pulsars and imaging H<sub>I</sub> simultaneously ([Li et al. 2018](#)), which enables a so-called deep Galactic-plane and Andromeda Survey (GAS). GAS will be sensitive to H<sub>I</sub> column density as low as  $5 \times 10^{16} \text{ cm}^{-2}$ , a significant improvement over all previous studies.

Many of the issues surrounding how to interpret M31's complex environment come down to an incomplete understanding of how it has interacted with M33, its most massive companion, in the last few billion years. A close interaction ( $< 100 \text{ kpc}$ ) in the past could in principle generate tidal features that survive today. However, a recent study based on new ESA *Gaia* proper motions (PM) of the Andromeda system appear to rule out this possibility ([van der Marel et al. 2019](#)). But this important study did not carry out a self-consistent dynamical simulation, i.e. they did *not* consider the problem of mass loss from either or both systems in their backwards integration. Whether two systems are on first infall or have experienced multiple orbits about each other cannot be reliably determined without consideration of mass loss ([Nichols & Bland-Hawthorn 2009](#)).

We revisit the orbital evolution of M31 and M33 with a more sophisticated treatment involving N-body/hydrodynamical simulations and forward-backward orbit integration, accounting for dynamical friction and dynamical mass loss in a self-consistent way. Our work presents the first self-consistent simulations of the Andromeda system to make use of the *Gaia* DR2 PM constraint. Earlier simulations (e.g. [McConnachie et al. 2009](#)) were constrained by outdated PMs and also targeted specific aspects of the rich structure observed around and around M31 ([Tanaka et al. 2010](#)). Notably, [Hammer et al. \(2018\)](#) attempt the first cohesive picture for the M31/M33 system using full N-body/hydrodynamical simulations but they concentrate on the stellar components. Our particular focus is the distribution of the extended gas around both M31 and M33, with a view to understanding the gas accretion history, and to aid our upcoming observations with the FAST telescope.

## 2 A NEW ORBITAL HISTORY OF THE M31/M33 SYSTEM

If one ignores their environment, the orbital history of two galaxies with respect to one another is governed by the following factors: 1) the mass distribution (i.e. the gravitational potential) of the galaxies; 2) the effect of dynamical friction (DF); 3) the effect of mass variation, generally mass loss due to tidal stripping. A widespread approach in inferring the orbital history of two galaxies with respect to one other is to take its present-day orbital parameters, and integrate the equations of motion backwards in time. In doing so, the galaxies are generally approximated by monolithic, extended bodies. We refer to this approach as 'semi-analytic orbit integration' (SAOI). This approach is a strict two-body orbit integration, and it therefore necessarily ignores the effects of dynamical friction and tidal stripping. These need to be accounted for using idealized parameterizations which themselves rely on a number of assumptions. A survey of the relevant literature reveals that, quite surprisingly, it appears to be a common practice to ignore the effect of tidal stripping altogether, with a few notable exceptions (e.g. [Jiang & Binney 2000](#); [Nichols & Bland-Hawthorn 2009](#); [Dierickx & Loeb 2017](#)).

The orbital history of the M31/M33 system has been repeatedly studied in the past in response to improvements in their proper motion (PM) measurements (e.g. [van der Marel et al. 2012b](#); [Salomon et al. 2016](#); [Patel et al. 2017](#)). Most recently, [van der Marel et al. \(2019\)](#) have explored the implications of the new *Gaia* DR2 PM for these galaxies. They concluded, as did [van der Marel et al. \(2012b\)](#) and [Patel et al. \(2017\)](#) before them using different PM data sets, that M33 is likely on its first approach to M31. However, their calculations ignore the effect of tidal stripping. Nor do these authors appear to calibrate their analytic calculations with corresponding N-body simulations. As we show, the latter is important given the assumptions that underly the calculation of the dynamical friction.

We calculate anew the orbital history of M33 around M31 accounting for the effect of dynamical friction and mass loss due to tidal stripping in a self-consistent way. To this end, we choose to use the *Gaia* DR2 PM alone (and not, say, the weighted *Gaia* / *Hubble Space Telescope* measurements; see [van der Marel et al. 2019](#)) since they represent the most extreme of the PM measurements in the sense that they have been claimed to *exclusively* support orbital histories where M33 is on its first approach to M31 ([van der Marel et al. 2019](#)). At the other extreme are the PM measurements by [Salomon et al. \(2016\)](#), which allow orbital histories with at least one close encounter between these galaxies with pericentric distances well below 100 kpc (e.g. [Semezuk et al. 2018](#)). It must be noted that the PM measurements by [Salomon et al. \(2016\)](#) are not consistent with the *Gaia* DR 2 PM measurements.

We shall ignore throughout the presence of additional members of the Andromeda group as well as the Milky Way and its satellites (e.g. LMC/SMC) and their gravitational perturbation of the M31/M33 orbit. As shown by [Patel et al. \(2017\)](#), this is a valid approximation.

Our SAOI approach is as follows.<sup>1</sup> The dynamics of the two-body system is governed by the following coupled 3D equation of motions:

$$\ddot{\vec{r}}_{31} = -\vec{\nabla}\phi_{33}, \quad (1)$$

$$\ddot{\vec{r}}_{33} = -\vec{\nabla}\phi_{31} + \vec{f}_{\text{DF}}, \quad (2)$$

<sup>1</sup> Our integration code is freely available upon request via email to the corresponding author (TTG).

where  $r \equiv |\vec{r}_{33} - \vec{r}_{31}|$  is the relative distance between M31 and M33; and  $\vec{f}_{\text{df}}$  is the acceleration due to dynamical friction, discussed below. The gravitational field is given by  $-\vec{\nabla}\phi_{31,33}(r) = -(GM_{31,33}(r)/r^2)\hat{r}$ . Here,  $G$  is the gravitational constant,  $\hat{r}$  is the unit vector in the direction of  $\vec{r}$ , and  $M_{31,33}(r)$  are the masses of M31 and M33 enclosed within  $r$ .

To obtain an orbital solution, we integrate the system of equations (1 - 2) backwards in time for roughly 8 Gyr using a leapfrog ('kick-drift-kick') scheme<sup>2</sup> with a fixed time step of  $\Delta t = 10^{-3}$  Gyr, accounting for the effect of dynamical friction and mass loss due to tidal stripping as described below.

Our orbital solution will depend on a number of factors: 1) the value of the orbital initial conditions; 2) the mass model of each galaxy; 3) the prescription to calculate the effect of dynamical friction; and 4) the prescription to account for the effect of tidal stripping. We describe each of these next.

The orbital initial conditions are set by the following present-day orbital parameters. The position of M33 relative to M31 is (van der Marel et al. 2012a; Semczuk et al. 2018)

$$\vec{r}_0 = (-97 \pm 23, -122 \pm 35, -130 \pm 19) \text{ kpc}, \quad (3)$$

corresponding to a present-day relative distance<sup>3</sup>  $d_0 = 203 \pm 27$  kpc. We adopt the central value of the velocity from the *Gaia* DR2 proper motion (PM) measurements alone (van der Marel et al. 2019),  $\vec{v}_{0,31} = (0 \pm 75, 176 \pm 51 - 84 \pm 73) \text{ km s}^{-1}$  and  $\vec{v}_{0,33} = (49 \pm 74, 14 \pm 70, 28 \pm 73) \text{ km s}^{-1}$ , which yield a relative velocity of

$$\vec{v}_0 = (49 \pm 105, 190 \pm 87, 112 \pm 104) \text{ km s}^{-1}, \quad (4)$$

corresponding to a present-day relative space velocity of  $v_0 = 226 \pm 92 \text{ km s}^{-1}$ , with a radial component of  $-209 \text{ km s}^{-1}$ , and a tangential component of  $85 \text{ km s}^{-1}$ . The uncertainty on these PM measurements is still large, but consistent within  $1\sigma$  with earlier measurements taken with the *Hubble Space Telescope* (HST; van der Marel et al. 2012b).

We approximate M31 and M33 each by a spherical DM halo, and ignore their other components (stellar bulge, stellar disc, gas disc, hot halo); see Table 2). Since the mass of each galaxy is dominated by its host DM halo, and the shortest relative distance between the galaxies is well beyond their optical radii along their common orbit, this approximation does not affect our orbital integration. Indeed, as we show in the next section, the orbital history we find with our SAOI approach agrees well with the corresponding result obtained from a pure N-body simulation – that does account for the full multi-component nature of the two galaxies –, thus indicating that the error introduced by our approximation is negligible. It is perhaps important to note that the total mass and its distribution both in M31 and M33 are still highly uncertain. This allows to choose suitable parameter values within a broad range consistent with observations.

Following Patel et al. (2017), M31's DM host halo is assumed to be well described by a Navarro et al. (1997, NFW) profile; the DM halo of M33 is approximated by a Plummer (1911) sphere. For the purpose of our SAOI, each galaxy model is fully specified by its total mass  $M_t$ , a scale radius  $r_s$ , and a truncation radius  $r_{tr}$  (see Table 2). The total mass of our M31 model is  $\sim 2 \times 10^{12} \text{ M}_\odot$  and of our M33 model,  $\sim 1.6 \times 10^{11} \text{ M}_\odot$ .

The mass of M31 is consistent with the upper limit of the mass

<sup>2</sup> This scheme is fully time-reversible, and thus appropriate to ensure that the backwards and forward integration of the orbit are consistent with one another. The adopted time step size is small enough to avoid energy drift.

<sup>3</sup> The total uncertainty is calculated assuming simple error propagation and uncorrelated measurement error among the coordinates.

of this galaxy based on limits to the total mass of the Local Group ( $\sim 3 \times 10^{12} \text{ M}_\odot$ ; e.g. Diaz et al. 2014, see also Fardal et al. 2013), and independent estimates of the mass of the Milky Way ( $\sim 1 \times 10^{12} \text{ M}_\odot$ ; e.g. McMillan 2017).

The mass of M33 we adopt is lower than traditional estimates based on the modeling of its observed rotation curve. Using this approach, Kam et al. (2017) estimate a virial mass for M33 of  $\sim 5 \times 10^{11} \text{ M}_\odot$  (see also Corbelli et al. 2014). As discussed by these authors, however, with a baryonic mass of order  $\lesssim 10^{10} \text{ M}_\odot$ , the baryonic:total mass fraction in M33 is only  $\lesssim 2\%$ , well below the typical value for disc galaxies ( $\sim 7\%$ ; e.g. Zaritsky et al. 2014). Estimates of the mass of a galaxy based on the rotation curve alone out to radii beyond the maximum observed extension are highly model dependent. If instead we assume the estimates of the total baryonic fraction to be more robust, then the average baryon:total mass fraction in disc galaxies implies a total mass for M33 at the present-epoch of  $\sim 1.5 \times 10^{11} \text{ M}_\odot$ , consistent with the value we adopt.

Given its larger mass, M31's DM halo is likely to be more extended than M33's at all times. Therefore, we assume that M33 experiences the effect of dynamical friction by the DM matter field of M31 but not vice-versa. This assumption is reflected in the form of equations (1 - 2). Following previous work, the acceleration due to dynamical friction is accounted for using a special case derived from the generic Chandrasekhar formula:

$$\vec{f}_{\text{df}} = -4\pi G^2 \ln \Lambda \rho_{31}^{\text{DM}} M_{33} \left\{ \text{erf}[\chi] - \frac{2\chi}{\sqrt{\pi}} \exp[-\chi^2] \right\} \frac{\vec{v}}{v^3}, \quad (5)$$

where  $\rho_{31}^{\text{DM}}(r)$  describes M31's DM density field;  $v \equiv |\vec{v}|$  is the relative velocity of M31 and M33;  $\text{erf}[\cdot]$  is the error function,  $\chi \equiv v/\sqrt{2}\sigma^{\text{DM}}(r)$ ; here,  $\sigma^{\text{DM}}(r)$  is the one-dimensional velocity dispersion of M31's DM matter field. The term  $\ln \Lambda$  is the Coulomb logarithm, discussed below.

It is worth keeping in mind the assumptions underlying equation (5). First, it is assumed that the mass of the DM particle is negligible compared to M33's total mass at any point along the orbit, i.e.  $M_{33}(r) \gg m_{\text{DM}}$ . Second, it is assumed that the velocities of the DM particles obey a Maxwellian distribution. While the former may seem reasonable, the latter may in fact not be justified in general.

The velocity dispersion is calculated using the analytic fit by Zentner & Bullock (2003):

$$\sigma^{\text{DM}}(r) = V_{\text{max}} \frac{1.4393 x^{0.354}}{1 + 1.1756 x^{0.725}}, \quad (6)$$

appropriate for an NFW profile and accurate to 1% in the range  $x = [10^{-2}, 10^2]$ . Here,  $x = r/r_s$  and  $V_{\text{max}}$  is the peak value of the circular velocity of the DM halo, which for an NFW profile is found at a distance from the centre  $r \approx 2.16r_s$ .<sup>4</sup>

The Coulomb logarithm is a measure of the scattering between the object experiencing dynamical friction and the background matter field responsible for the latter. The Coulomb logarithm is, in fact, unknown in most cases of interest in galactic dynamics, and a number of parameterizations are known. We adopt Hashimoto et al. (2003)'s,  $\ln \Lambda = r/1.4\epsilon$ . Here,  $\epsilon$  is the so-called 'softening length', usually taken to be the (equivalent) Plummer scale radius of the mass model. It is a free, and thus a tunable parameter. Its value can only be guessed, and it is best set via a trial-and-error approach in an iterative way comparing the outcome of the SAOI

<sup>4</sup> In practice, we use a root finding algorithm to obtain  $V_{\text{max}}$ .

and a corresponding N-body simulation.<sup>5</sup> As discussed in the next section, the value that leads to the best match between our SAOI and a N-body simulation is  $\epsilon \approx 3.6$  kpc. It is worth noting that, somewhat ironically, the latter value is roughly a fraction 1/5 of the value of the Plummer scale radius we use for M33's mass model (see Table 2).

As mentioned earlier, a key difference between our approach and similar previous work is that we take into account the effect of mass loss due to tidal stripping. We assume that only M33 experiences the effect of stripping by the tidal field of M31. This implies that M31's mass is constant during the orbital evolution of the two galaxies, and it does not require any special treatment during the approach outlined below.

Following Nichols & Bland-Hawthorn (2009), tidal stripping is implemented as follows. First, we calculate the tidal radius  $r_t$  of M33 at each time step via (Klypin et al. 1999)

$$\left(\frac{r}{r_t}\right)^3 \frac{M_{33}(r_t)}{M_{31}(r)} = 2 - \frac{r}{M_{31}(r)} \frac{dM_{31}(r)}{dr}. \quad (7)$$

Usually, one assumes that the mass beyond the tidal radius is lost at any point along the orbit, in particular at each pericentric passage (because the tidal radius is smallest there).<sup>6</sup> But this is a valid assumption only when moving *forward* in time along the orbit. A critical aspect in our approach is how to handle the effect of tidal stripping when integrating *backwards* in time. The inverted time arrow implies that mass has to *increase*. This is indeed a non-trivial task because calculating the bound mass at each pericentric passage recursively requires knowledge of the earlier (in time) bound mass (or the earlier pericentric distance), which is impossible unless the full orbit is known in advance.

Our strategy to tackle this difficulty is as follows. We assume an arbitrary reference mass and a present-day (initial) bound mass for M33. We integrate the orbit until we identify the first pericentric passage (if any) along the orbit, and calculate there the tidal radius and the corresponding bound mass of M33 using the reference mass. The new bound mass is then set to the maximum of the previous and the new bound masses, which ensures that M33's mass is a monotonically increasing function along the backwards orbit.

The previous steps are repeated until the integration time is reached. The last bound mass obtained defines M33's infall mass. Its value is used together with its corresponding orbital parameters as input for a forward integration. When integrating forward in time, we ensure that whenever the tidal radius increases (as a result of an increased relative distance between the galaxies), the bound mass does not increase. In other words, M33's mass is a strictly monotonically decreasing function along the forward orbit – i.e. the inverse behaviour of M33's mass when integrating backwards.

We note that the use of a reference mass renders our approach not fully self-consistent at first because, during a backwards integration, the potential of M33 is defined by the reference mass, while the mass that enters into the calculation of the dynamical friction force is given by the bound mass at that point along the orbit. To guarantee self-consistency, one needs to make sure that the final (i.e. present-day) mass resulting from the forward integration matches (as closely as possible) the initial bound mass used for the backwards integration. Consistency with observations dictates the initial

<sup>5</sup> Other authors adopt slightly different values for the constant factor in the denominator. This is irrelevant since it is the product of this factor and  $\epsilon$  that determines the behaviour of this particular parametrization of  $\ln A$ .

<sup>6</sup> The tidal radius is implicitly defined in equation (7) and it needs to be solved for with a root finding algorithm. We use the Brent method.

bound mass be given by the value of M33's present-day mass. The reference mass is thus the only free parameter in our approach to account for dynamical mass loss. The sole constraint on it is that it must be larger than the present-day mass of M33. It is important to realize that the reference mass is simply an auxiliary quantity that has not physical meaning and that plays no role in the final orbital solution once this has been found. In particular, the reference mass does not enter the calculation of the forward orbit.

Following a simple trial-and-error approach, and with some intuition, it does not take a large number of attempts to find the value of the reference mass such that the value of the infall and the final bound masses of M33 obtained during the backwards integration are consistent with their corresponding values obtained during the corresponding forward integration.<sup>7</sup> We find that a reference mass for M33 of  $3.55 \times 10^{11} M_\odot$  yields a backwards (forward) infall mass of  $2.31 \times 10^{11} M_\odot$  ( $2.63 \times 10^{11} M_\odot$ ); and a backwards (forward) final mass of  $1.31 \times 10^{11} M_\odot$  ( $1.56 \times 10^{11} M_\odot$ ); the latter are both consistent with the our estimate for the present-day mass of M33 ( $\sim 1.5 \times 10^{11} M_\odot$ ; see above).

Using these values together with our best value for  $\epsilon$ ,<sup>8</sup> a backwards integration of the M31/M33 system by roughly 8 Gyr into the past constrained by their present-day orbital parameters (eqs. 3 and 4) yields a relative infall position between the galaxies  $\vec{r}_{-8} = (-321, 306, -172)$  kpc, corresponding to an infall relative distance of 475.7 kpc, and a relative infall velocity  $\vec{v}_{-8} = (175, -107, 116)$  km s<sup>-1</sup>, corresponding to an infall relative speed 235.3 km s<sup>-1</sup>.

The results from our SAOI calculation just described are displayed in Fig. 1. The left panel shows the orbital histories that result from a backwards integration accounting for the effect of tidal stripping (crosses;  $\times$ ) or without it (dashed curve). The latter result is virtually identical to the orbital history calculated by Patel et al. (2017, see their ‘high-mass M31/high-mass M33’ result), which corresponds to a ‘first-infall’ scenario.

The right panel of Fig. 1 displays the distance (top) and the speed (bottom) between M31 and M33 along their common orbit. The observed relative distance and the observed relative speed are indicated in each case by the horizontal dashed line and the shaded area. The full 3D information is displayed in Tab. 1. Both the relative distance and the relative speed resulting from our SAOI calculation match their observed counterpart well within their corresponding uncertainty.

Our time integration (leapfrog) scheme is time-reversible by construction (even accounting for the effect of dynamical friction), and now we show that our prescription to account for mass loss via tidal stripping is as well. In the left panel of Fig. 1 we visually compare the result from our forward (solid curve) and backward (crosses;  $\times$ ) calculations. The agreement between these indicates that our backwards and forward orbital calculations are consistent with each other. It also shows that the reference (auxiliary) mass has no effect on the forward orbital solution, as claimed above.

The striking difference between the orbit indicated by the crosses (henceforth referred to as ‘second infall’) and the dashed curve (‘first infall’) displayed in the left panel of Fig. 1 demonstrates that the effect of mass loss due to tidal stripping significantly

<sup>7</sup> This procedure can be automated using a suitable iterative algorithm. We defer this task to a future work.

<sup>8</sup> It is worth emphasizing that the values of the reference mass and  $\epsilon$  are particular to the orbital parameters and to the galaxy mass distributions considered here, and there is guarantee that, nor an obvious reason why, these values should be valid in general.

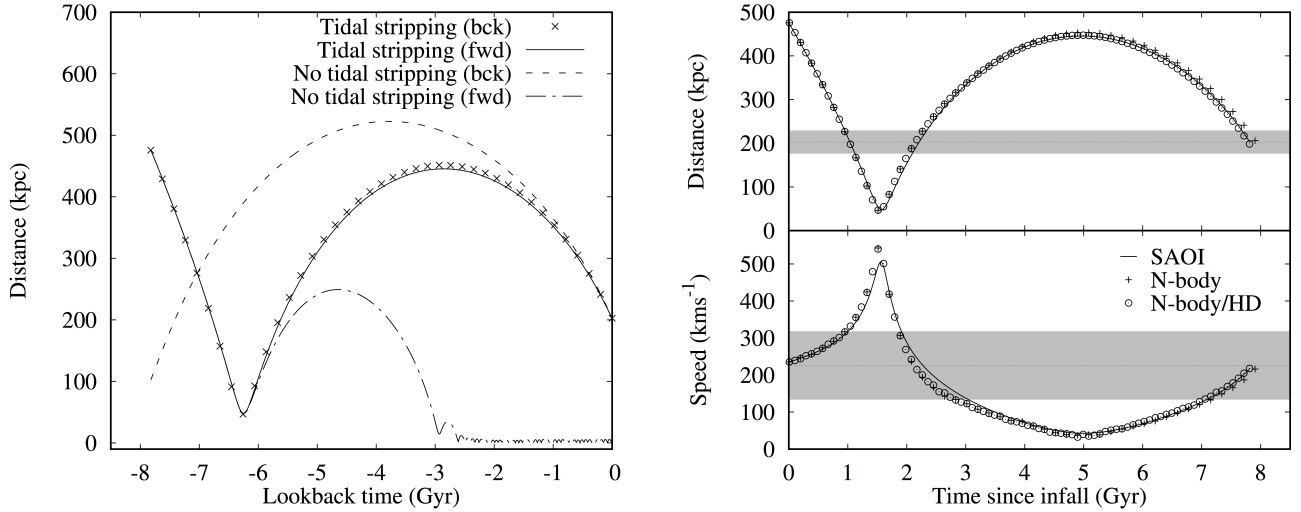


**Figure 1.** Orbital history of the M31/M33 system. Left: A comparison of the orbital history obtained with a backwards ('bck') or forward ('fwd') SAOI with/without tidal stripping. Note that the solid curve overlaps with the dot-dashed curve from infall (at  $\sim 8$  Gyr in the past) up to the pericentric passage. The infall epoch and the present-day are flagged by a look-back time of  $\tau = -8$  Gyr and  $\tau = 0$  Gyr, respectively. Right: Relative distance (top) and relative speed (bottom) between M33 and M31. The solid curves correspond to the result of our forward SAOI calculations. The plus signs (+) and the open circles ( $\odot$ ) correspond to the distance (top) and speed (bottom) between M31 and M33 in a N-body simulation and a full N-body/hydrodynamical simulation, respectively. The gray-shaded area indicates either the observed relative distance or the observed relative speed and its associated uncertainty. In this panel, the infall epoch and the present-day are indicated by  $t = 0$  Gyr and  $t \approx 8$  Gyr, respectively. Note that the orbital history indicated by the solid curve in the left panel is identical to that indicated by the solid curve in the top sub-panel on the right.

**Table 1.** Infall- and present-day parameters. All values correspond to properties of M33 relative to M31. In all cases the relative position at infall ( $\sim 8$  Gyr in the past) is  $\vec{r}_{-8} = (-321, 306, -172)$  kpc, corresponding to a relative distance of 475.7 kpc, and the relative velocity at infall is  $\vec{v}_{-8} = (175, -107, 116)$  km s $^{-1}$ , corresponding to a relative speed 235.3 km s $^{-1}$ . Position and distances in kpc; velocities and speeds in km s $^{-1}$ . No errors given for results other than those obtained from observations.

	Position $\vec{r}_0 = (x, y, z)$	Distance	Velocity $\vec{v}_0 = (v_x, v_y, v_z)$	Speed
Observations / data	$(-97 \pm 24, -122 \pm 35 - 130 \pm 19)$	$203 \pm 27$	$(49 \pm 105, 190 \pm 87, 112 \pm 104)$	$226 \pm 92$
SAOI	$(-86, -133, -124)$	201	$(37, 190, 101)$	219
N-body	$(-66, -163, -140)$	224	$(4, 186, 71)$	199
N-body/HD	$(-64, -139, -126)$	198	$(14, 201, 83)$	218

changes the nature of the orbital solution. This result is the interplay between two factors: 1) the higher initial (i.e. present-day) mass of the first-infall orbit ( $\sim 2.6 \times 10^{11} M_{\odot}$ ) compared to the second infall orbit ( $\sim 1.6 \times 10^{11} M_{\odot}$ ); 2) the reference mass needed to calculate the second-infall solution. The former affects the behaviour of the dynamical friction force. The latter affects the effective gravitational pull between the galaxies. Nonetheless, we stress that the reference mass has no physical meaning, and does not enter the calculation of the forward orbital evolution, once a solution has been found.

The effect of tidal stripping is truly apparent in the forward orbital history (Fig. 1, left panel). The dot-dashed curve shows the orbit resulting from identical initial conditions (infall mass, orbital parameters) as used in the second-infall solution (solid curve), but ignoring the effect of tidal stripping. Clearly, the resulting orbital histories are identical up to a few million years after the pericentric passage. As a result of tidal stripping there, M33 loses roughly half its mass, and the effect of DF becomes smaller, thus allowing the

galaxy to reach a greater distance from M31. In contrast, ignoring mass loss due to tidal stripping yields a stronger DF effect and thus a stronger orbital decay. So strong in fact that M33 undergoes a number of additional pericentric passages before merging with M31.

It is important to realize that both orbital solutions, first- and second-infall, are in fact possible. Without further knowledge about the true mass evolution of M33, there is no objective preference for one over the other. However, the orbital solution with a pericentric passage well below 100 kpc consistent with the *Gaia* PM DR2 is a result which was so far considered to be ruled out. We note that orbital solutions with close encounters ( $< 100$  kpc) are in fact known (Semczuk et al. 2018), but these results precede the *Gaia* DR2 PM measurements, and are based on orbital parameters which are not consistent with the latter.

In summary, with a full account of the relevant physical processes at play (gravity, dynamical friction, tidal stripping) we have

found a new orbital solution in which M33 underwent a close ( $\lesssim 50$  kpc) pericentric passage from M31's centre roughly 6.5 Gyr ago. The question then arises of how this close encounter affected the evolution of these galaxies, and whether there are fossil imprints of this interaction still observable today. In order to address this question, we resort to a full N-body/hydrodynamical simulation of the infall of M33 into M31.

### 3 THE INFALL OF M33 INTO M31

Prior to exploring the consequences that the orbital history we have found, we need to ensure we can recover our SAOI solution with a full N-body/hydrodynamical simulation. This is a necessary step given the simplifying assumptions underlying our SAOI calculation, in particular the idealized form of the dynamical friction and the prescription to account for dynamical mass loss. For now we opt to address this in an iterative way, as described below.<sup>9</sup> Because N-body/hydrodynamical simulations are expensive, we choose to use first pure N-body simulations.

#### 3.1 A minimal N-Body model

Dynamical friction and tidal stripping are naturally and self-consistently accounted for in N-body simulations. Thus, for a given set of initial orbital parameters the most important factors determining the outcome of a N-body simulation of the infall of M33 into M31 is the mass model used to approximate each of these galaxies.

We assume both M31 and M33 are multi-component systems each consisting a stellar disc embedded within a host DM halo. In addition, M31 is assumed to host a stellar bulge, as observed (q.v. [Mould 2013](#)). The adopted profile and structural parameters for each of the components of each galaxy are given in [Tab. 2](#). Note the we ignore the gaseous components for now. These will be taken into account in our full N-body/hydrodynamical simulation discussed in the next section.

Other physical factors that likely affect the outcome of an N-body simulation include the initial orientation of the galaxy spins relative to their orbit. Following [Semczuk et al. \(2018\)](#), M31's spin is initially pointing along the  $z$ -axis; the spin of M33 is initially pointing the negative  $x$ -axis.

To follow the simplest approach possible, we consider  $\epsilon$  to be the only free parameter of our SAOI calculation. With this assumption, we proceed to verify our semi-analytic as follows. First, we obtain the infall orbital parameters obtained from a backwards integration adopting a first guess for the value of  $\epsilon$ . A common choice is to set  $\epsilon$  to the (equivalent) Plummer scale length of M33's mass model (see [Tab. 2](#)). Then, we use these orbital parameters and a N-body representation of M31 and M33 (see next section) to run a simulation forward in time. We then compare the orbital history of M33 relative to M31 obtained in the simulation to the SAOI result. In the likely event that no good agreement is found, we tune the value of  $\epsilon$  and repeat the previous steps until a good match between our SAOI calculation and the N-body simulation is obtained. Our best value thus obtained is  $\epsilon \approx 3.6$  kpc. The infall orbital parameters obtained from the backwards integration at  $\sim 8$  Gyr in the past are  $\vec{r}_{-8} = (-321, 306, -172)$  kpc, and  $\vec{v}_{-8} = (175, -107, 116)$  km s $^{-1}$ .

The orbital history that results from our N-body simulation is displayed in the right panel of [Fig. 1](#) and is indicated by the plus

<sup>9</sup> See [Footnote 7](#).

signs (+), along with the corresponding results from our forward semi-analytic integration (solid curve). The values of the corresponding 3D position and the 3D velocity are given in [Tab. 1](#). The relative position and the relative velocity of the galaxies in our N-body simulation are calculated by estimating the centre of mass and centre of velocity of each galaxy's stellar disc at each time step.<sup>10</sup> We do this in an iterative way until their respective value convergence within some tolerance to take into account strong anisotropies in both the mass and the velocity distribution caused by tidal distortion. The calculation of the centre of velocity is performed in the same way. However, it is bears the additional complication that the velocity of the individual stars is superimposed on the barycentre's motion as they revolve around the potential's centre. This explains the larger departure of the relative speed relative to the SAOI result. In contrast, the relative position in the N-body model faithfully follows the SAOI result.

The results of [Fig. 1](#) and [Tab. 1](#) demonstrate that orbital history obtained from our N-body simulation are consistent with the SAOI result. This is indeed remarkable considering all the simplifying assumptions factored into our SAOI calculations. It must be mentioned though that the difference between the present-day orbital parameters obtained from our N-body simulation and their observed counterpart is larger than the difference between the latter and our SAOI result. Nonetheless, we are confident that the physical processes at play relevant to the dynamical evolution of the M31/M33 system (gravity, dynamical friction, tidal stripping) are captured correctly in our N-body model. We believe that extensive tuning of the free parameters of the model (galaxy masses; their spin orientation, of each galaxy;  $\epsilon$ , etc.) – constrained by observations where possible – may yield a better match between a N-body simulation and the present-day orbital parameters of the M31/M33 system. A more thorough exploration of the orbital parameter space is left for future work.

Thus we consider the agreement between the observed present-day orbital parameters of the M31/M33 system and the result from our N-body model good enough for our present purpose, and proceed to model the infall of M33 into M31 using a full N-body/hydrodynamical simulation.

#### 3.2 A full gas-dynamical model

In our N-body/hydrodynamical model, each of the galaxies is assumed to host, in addition to the collisionless components described above, a gas disc. [Semczuk et al. \(2018\)](#) demonstrated the importance of a hot halo around M31 in order properly account for the effect of ram pressure onto the gas around M33. Therefore, our M31 model includes a hot halo as well. We note that [Semczuk et al. \(2018\)](#) did not specify the metallicity of the hot halo (M31) or the gas disc (M33). This is important if the effect of radiative cooling of the gas is accounted for, as we do. Guided by the corresponding values of the Milky Way ([Miller & Bregman 2015; Hou et al. 2000](#)), we adopt a value of 0.3 solar for the metallicity of the M31's gas components, and a slightly lower value of 0.2 solar for M33's gas disc. The galaxies are embedded in a diffuse background medium with a mean temperature  $\sim 10^6$  K and a density  $\sim 10^{-7}$  cm $^{-3}$ .<sup>11</sup>

<sup>10</sup> Using the position of centre of mass of their respective DM halo yields virtually identical results.

<sup>11</sup> The latter is likely significantly lower than the mean density of the intergalactic medium (IGM) in the Local Group. We adopt such a low value in order to deter the gas filling the simulation volume from collapsing over

**Table 2.** Relevant model parameters (initial values). Column headers are as follows:  $M_t$  := total mass ( $10^9 M_\odot$ );  $r_s$  := scalelength (kpc);  $r_{tr}$  := truncation radius (kpc);  $N_p$  := particle number ( $10^5$ );  $Z$  := gas metallicity ( $Z_\odot$ ).

	Profile	$M_t$	$r_s$	$r_{tr}$	$N_p$	$Z$
M31						
DM halo	NFW	1910	11.7	326	10	–
Stellar bulge <sup>a</sup>	H	11.2	1	4	1	–
Stellar disc <sup>a</sup>	Exp	80.7	7.3 <sup>c</sup>	40	10	–
Hot halo	NFW	3.10	11.7	326	–	0.3
Gas disc	Exp <sup>b</sup>	7.2 5	5.0 <sup>d</sup>	60	–	0.3
M33						
DM subhalo	Plu	262	17.9	197	10	–
Stellar disc <sup>a,f</sup>	Exp	5.8	2.5 <sup>e</sup>	25	5	–
Gas disc	Exp <sup>b</sup>	5.8	2.5	40	–	0.2

Notes. NFW, [Navarro et al. \(1997\)](#) profile; H, [Hernquist \(1990\)](#) profile; Plu, [Plummer \(1911\)](#) profile; Exp, Radial exponential profile

<sup>a</sup>The stellar metallicity is ignored as it is of no relevance for our study.

<sup>b</sup>In vertical hydrostatic equilibrium initially at  $T = 10^4$  K

<sup>c</sup>Scaleheight set to 1 kpc.

<sup>d</sup>Scaleheight set by vertical hydrostatic equilibrium ('flaring' disc).

<sup>e</sup>Scaleheight set to 0.5 kpc.

<sup>f</sup>Toomre's  $Q > 1.8$  everywhere initially ([Tenjes et al. 2017](#))

We generate the pure N-body and the N-body+gas representations for each galaxy with the DICE code ([Perret et al. 2014](#)). The corresponding initial conditions – both the pure N-body and the N-body/HD run – are evolved with the RAMSES code (version 3.0 of the code last described by [Teyssier 2002](#)). The limiting spatial resolution in our simulations is  $\gtrsim 60$  pc at all times. The mass resolution for each component can be easily obtained from Tab. 2, columns 3 and 6.<sup>12</sup> Our full N-body/hydrodynamical simulation includes the effect of radiative cooling of the gas by hydrogen, helium and heavy elements, and heating by the cosmic ultra-violet radiation background, but it does not include additional sub-grid physics such as star formation or feedback of any kind. This implies that our model as is cannot be used to make any statements about the details of the ionization state of the gas, or the details (formation, age, chemical composition and its distribution) of the stellar components of the galaxies. We kindly refer the reader to our previous work ([Tepper-García et al. 2019](#), and references therein) for more details on our simulation technique.

Full rendered animations of the evolution of the M31/M33 system can be found at [http://www.physics.usyd.edu.au/~tepper/proj\\_m31m33.html](http://www.physics.usyd.edu.au/~tepper/proj_m31m33.html).

#### 4 TIDAL STRUCTURES: ECHOES OF A PAST INTERACTION

The stellar halo of the Andromeda galaxy features a rich variety of structures which are likely the result of an extended period of

the course of the simulation. Alternatively, one could set the IGM to be in hydrostatic equilibrium. However, such a practice requires to specify a background potential, and this would only introduce additional and unconstrained parameters into the model.

<sup>12</sup> The setup files used to create initial conditions as well as those containing further details about the simulations are freely available upon request to the corresponding author (TTG).

interaction with and accretion of smaller systems. The most massive of these structures, the Giant Stellar Stream ([Ibata et al. 2001](#)), extends well beyond a projected distance of 40 kpc from M31's central region along the line towards M33. Using N-body models, [Fardal et al. \(2006\)](#) have attributed the origin of this structure to the recent interaction ( $\sim 750$  Myr ago) of M31 with a relative small companion ( $M \sim 10^9 M_\odot$ ). However, in view of the new orbital history presented here, it is worth exploring whether a close encounter with M33 in the distant past may have left its imprint in the form of a similar structure.

The distribution of gas around M31 strongly suggests that this galaxy has had a number of interactions with its companions. Above all, the H $\alpha$  filament along the projected line linking M31 with M33 ([Braun & Thilker 2004; Lockman et al. 2012; Kerp et al. 2016](#)) is of particular interest. This gaseous structure has been interpreted as either resulting from an interaction between these two galaxies (e.g. [Bekki 2008](#)) or the product of condensation within an intergalactic filament ([Wolfe et al. 2013, 2016](#)). The latter interpretation has gained support lately as a result of the claims that M33 may be on its first approach to M31 (e.g. [van der Marel et al. 2019](#)). Our new orbital solution featuring a close encounter between these galaxies is at odds with this claim, and thus renders the interaction scenario a plausible origin for the H $\alpha$  filament, as we discuss next.

#### 4.1 Stellar morphologies

The present-day distribution of stars and gas in the simulated M31/M33 system is displayed in Fig. 2 projected along three orthogonal directions. This choice has no other motivation than simplicity. While none of the resulting views fully matches the configuration of M31/M33 as seen on the sky, this is of no concern as we still have not exploited the freedom given by the isotropy of the simulation volume, which allows us to rigidly rotate the  $xyz$ -coordinate system in whichever way we see fit, nor have we adjusted the relative orientation of the initial spin of each galaxy with respect to their infall orbital parameters. With this in mind, we proceed with a qualitative comparison between our simulation results and observations.

The most apparent characteristics of the simulated M31/M33 systems visible in the top row of Fig. 2 are the lack of notorious stellar substructure around M31. In contrast, M33 displays a number of tidal stellar features. The close encounter between these galaxies in our model does result in both systems displaying strong tidal features around each other shortly thereafter. But M31 settles quickly so that it appears fairly undisturbed today, in contrast to observations. In particular, the simulated M31 does not display a structure reminiscent of the Giant Stellar Stream. Since we have ignored the presence of M31's satellites other than M33, the disagreement between our model and the data suggests, as have concluded other before us, that most of the stellar substructure around M31 observed today is due to interactions with its other satellites (e.g. [Fardal et al. 2006; Williams et al. 2015; Hammer et al. 2018](#)).

#### 4.2 Gas streams

The simulated M31/M33 displays a spectacular gas distribution (Fig. 2, bottom row). Both galaxies show tidal gas streams around them, extending for at least tens of kpc from their respective centre. Yet, the gas distribution around M31 appears more settled compared to M33, as does its stellar component (see previous section). The prominent gas stream extending from M31 away from M33 is reminiscent of the H $\alpha$  stream detected north-west of M31 (see [Braun & Thilker 2004](#), their figure 9; [Wolfe et al. 2016](#), their figure 1).

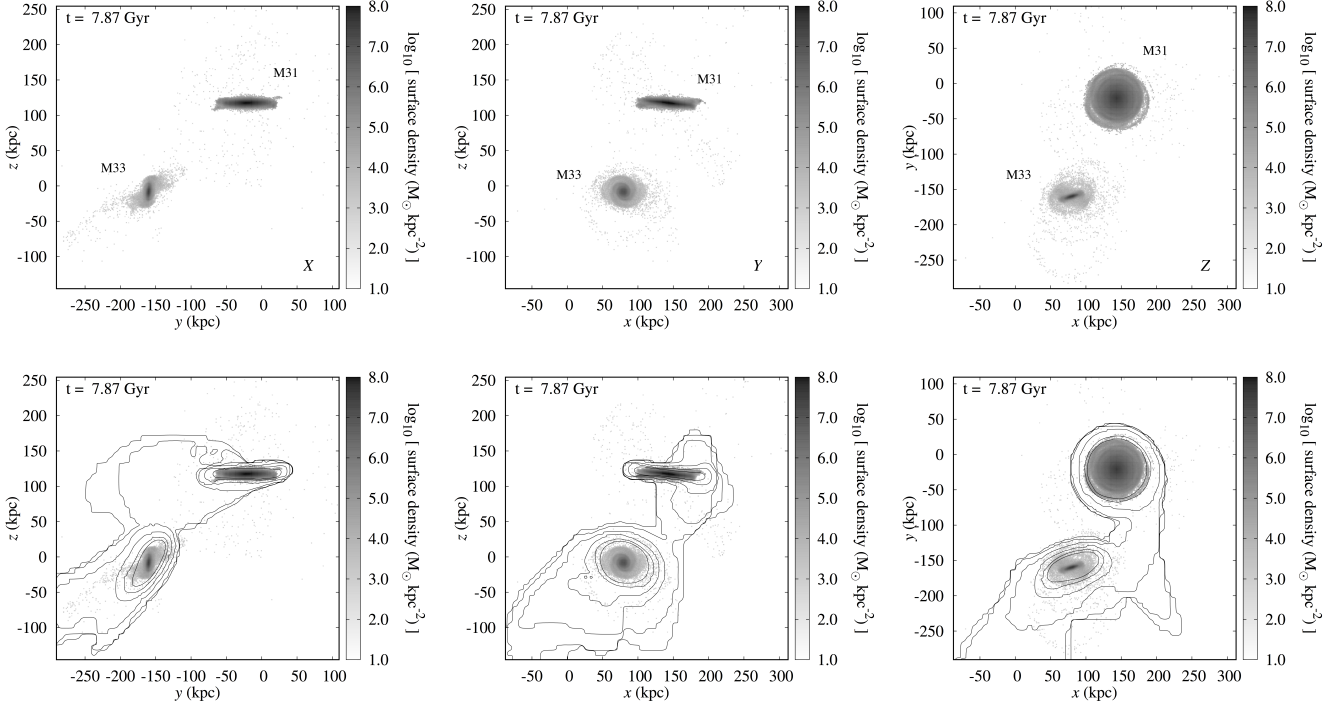


**Figure 2.** Distribution of stars and gas in the simulated M31/M33 system at the present epoch, i.e.  $\sim 7$  Gyr after M33 first crossed M31’s virial radius. From left to right, each column corresponds to the full 3D state of the system projected along the  $x$ -,  $y$ -, and  $z$ -axis, respectively. Top row: Distribution of stars from both M31 (visible in the top right corner in each panel) and M33 (in the bottom left corner of each panel). The gray scale indicates the value of the stellar surface density. Bottom row: Same as the top row but total gas column density contours overlaid. The contour levels indicate, starting from the innermost, a total gas column density  $\log[N_{\text{gas}}/\text{cm}^{-2}] = 19 - 17$  in steps of 0.4 dex. Only the gas initially bound to either M31 or M33 is included. The galaxy tags have been omitted for clarity. Note that the coordinate frame has its origin at the initial (i.e. at the start of the simulation) position of M31.

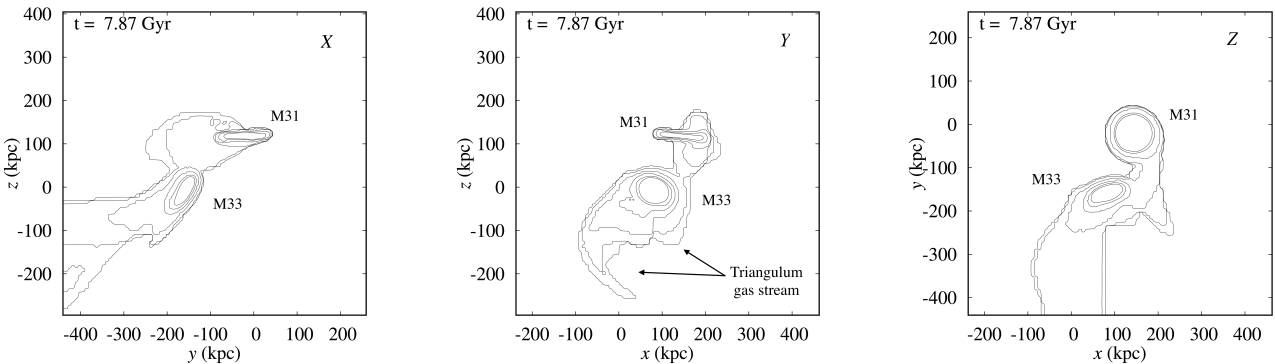


**Figure 3.** Distribution of gas in the simulated M31/M33 system at the present epoch, i.e.  $\sim 7$  Gyr after M33 first crossed M31’s virial radius, and  $\sim 6.5$  Gyr since their closest encounter. From left to right, each column displays the density of gas projected along the  $x$ -,  $y$ -, and  $z$ -axis, respectively. The contour levels indicate, starting from the innermost, a total gas column density  $\log[N_{\text{gas}}/\text{cm}^{-2}] = 19 - 17$  in steps of 0.4 dex. Note that the contours in each panel are identical to the contours displayed in the corresponding panel of the bottom row in Fig. 2, but projected on a larger physical scale. The gas corresponds to the gas initially bound to M31 and M33. The prominent, diffuse gas structure extending from M33 away from M31 referred to as the ‘Triangulum stream’ is yet to be observed. The stream has been tagged in the central panel only but it is clearly visible in the other projections as well. Note that the coordinate frame has its origin at the initial (i.e. at the start of the simulation) position of M31.

A panoramic view of the gas around the simulated M31/M33 system is shown in Fig. 3. M31 features a second prominent stream which extends all the way to M33, akin to the observed M31-M33 H<sub>1</sub> filament, without a stellar counterpart. We note that the formation epoch of this gas bridge dates back to the epoch of the close

encounter between the galaxies, and apparently survived up to the simulation present-day.

In addition to the gas bridge between the galaxies, M33 features a gas stream that trails from the galaxy for over 100 kpc – henceforth referred to as the ‘Triangulum stream’. This gas stream is not apparent in any of the H<sub>1</sub> maps available to date, although it

may be discernible in the data presented by [Putman et al. \(2009\)](#). Our model suggests that the Triangulum stream is very diffuse, with a *total* gas column density of  $\lesssim 10^{18} \text{ cm}^{-2}$ . Thus, we speculate that, if real, it has not been observed in H I emission because of its low H I column density, which may result from an overall low gas column density and/or a high ionization fraction of the gas; or because its distribution could be clumpy ([Bland-Hawthorn et al. 2017](#)). However, without an appropriate treatment of the ionization state of the gas accounting for its chemical composition, for the ionization field of the M33 and for the ultra-violet background, and a sufficiently high grid resolution, we cannot as yet make a more quantitative statement about the H I content of the Triangulum stream. Such an endeavor extends beyond the scope of the present paper and is left for future work.

The reason for the more extended distribution of gas compared to the stars, and the existence of gas streams with no stellar counterpart is that, in addition to tidal forces, the gas is subject to hydrodynamic forces exerted by the IGM as the galaxies move along their common orbit. Therefore, the properties of the gas streams will depend on the properties of the IGM. In particular, a IGM significantly denser than we have adopted in our model will likely yield to the formation of denser trailing tidal gas streams, and weaker leading ones as a result of the enhanced ram pressure ahead of the galaxy.

The initial extension of the gas disc relative to the stellar disc may also play a role in the different configuration of gas streams relative to stellar streams. Thus, while most of the stars sit close to the potential's centre, a non-negligible fraction of the gas is loosely bound and gets more easily stripped.

In our model we have assumed indeed very extended gas discs ( $\gtrsim 40 \text{ kpc}$ ) for both galaxies. In the case of M31, this does not seem implausible, given that the Milky Way is believed to have a gas disc that extends out to  $\sim 60 \text{ kpc}$  ([Kalberla & Kerp 2009](#)). The H I disc of M33 is observed to extend at least out to  $\sim 25 \text{ kpc}$  ([Corbelli et al. 2014](#)), and it is not unreasonable to assume that its ionized edge may extend beyond that ([Bland-Hawthorn et al. 2017](#)). It is also plausible that its extension at infall was much larger than that.

To sum up, our model indicates that the Giant Stellar stream is unlikely the result of an encounter in the distant past between M31 and M33. But the H I filament can be naturally explained in this scenario, at least qualitatively. Our model suggests that this structure is ancient, dating back to the epoch of the close encounter between the galaxies. Incidentally, our model predicts the presence of a yet to be observed gas stream, the Triangulum stream, that trails M33 as it falls into M31.

#### 4.3 The morphology of M33

Although somewhat beyond the scope of our present study, we would like to highlight some interesting features in the morphology of the simulated M33. First, it is worth noting the difference in its stellar morphology between the pure N-body model and the full gas-dynamical model. In the former, M33 quickly forms a bar shortly after its close encounter with M31 which survives up to the present day in the simulation (Fig. 4, top row). In contrast, in the N-body/HD model M33 never develops a bar (Fig. 4, bottom row). This suggests that the presence of gas stabilizes the disc against bi-symmetric ( $m = 2$ ) instabilities.

The apparent well-settled state of M33 has recently been revisited by [Sellwood et al. \(2019\)](#). Performing an extensive study using N-body/hydrodynamical simulations, they have found that any dynamical model constrained by M33's observed properties is

unstable to the formation of a strong bar within a short time-scale. But these models consider M33 only in isolation. Our result suggest that the gravitational influence of M31 may somehow stabilize M33, although it is unclear at the moment what could be the mechanism responsible for this effect.

The simulated M33 in our full N-body/HD run displays a warp both in its stellar disc and in its the gas disc (Fig. 5), as observed. It is interesting however that while the warp of the gas disc and the stellar tidal streams roughly align with each other along one projection, they appear anti-aligned along a different one (cf. left and right panels in Fig. 5). These configuration is likely particular to our initial orbital parameters and the spin orientation of M33 relative to its orbit. Nonetheless, these results highlight the complexity of the structure that results even in the simplest of models.

We close this section by noting that [van der Marel et al. \(2019\)](#) argue, reasonably, that in lack if a close encounter, the stellar and gaseous warps and tails of M33 cannot be the result of tidal forces. This in turn poses a puzzle on the origin of M33's disturbed morphology. However, as we have shown, these structures could naturally be explained within an interaction scenario (see also [McConnachie et al. 2009; Semczuk et al. 2018](#)). The influence of tidal forces may even explain the present-day stability of M33, so far considered a puzzle.

## 5 CONCLUDING REMARKS

Our new orbital history is only one out of potentially many possible orbital histories. Because of the somewhat laborious steps involved in our orbit calculation we have refrained for the moment to perform a more extensive exploration of the orbital parameter space. Nonetheless, given that our result is based on the central values of the orbital velocity measurements, it seems reasonable to expect that the family of orbits allowed by the uncertainty in these measurements will cluster around our orbital solution.

Previous studies ([Patel et al. 2017; van der Marel et al. 2019](#)) have shown that a lighter M33 disfavors orbits featuring a close encounter with M31. [van der Marel et al. \(2019\)](#) also show that the *Gaia* DR2 PM measurements alone are the most extreme in the sense that they exclusively support orbital histories where M33 is on its first approach to M31. We have adopted the lighter of the M33 models considered by these studies, in addition to the PM measurements that were thought to be the less likely to support orbital histories with a close encounter. Thus we conclude that orbital calculations which adopt a heavier M33 or use a different set of PM measurements would likely yield many more orbital solutions that allow for a close encounter between these galaxies.

We do not claim that M33 has with certainty had a past interaction with M31. We simply show that, constrained by the most recent PM measurements, an orbital history with a close encounter is plausible if the relevant physical processes involved are accounted for. The orbital solution we have presented here is a proof by counter-example, as it were, that the claim about M33 being on its first approach to M31 does not hold in general.

Our orbital calculations is relevant in two important aspects: 1) It shows that including the effect of dynamical mass loss – commonly ignored – can expand the space of solutions to a regime that was previously thought unaccessible.; 2) It shows that assumptions generally adopted about the value of parameters such as  $\epsilon$ , etc. which enter the semi-analytic calculation of the orbit, and which are not well understood, do not necessarily hold. In this respect, we stress the importance of N-body simulations to validate the results

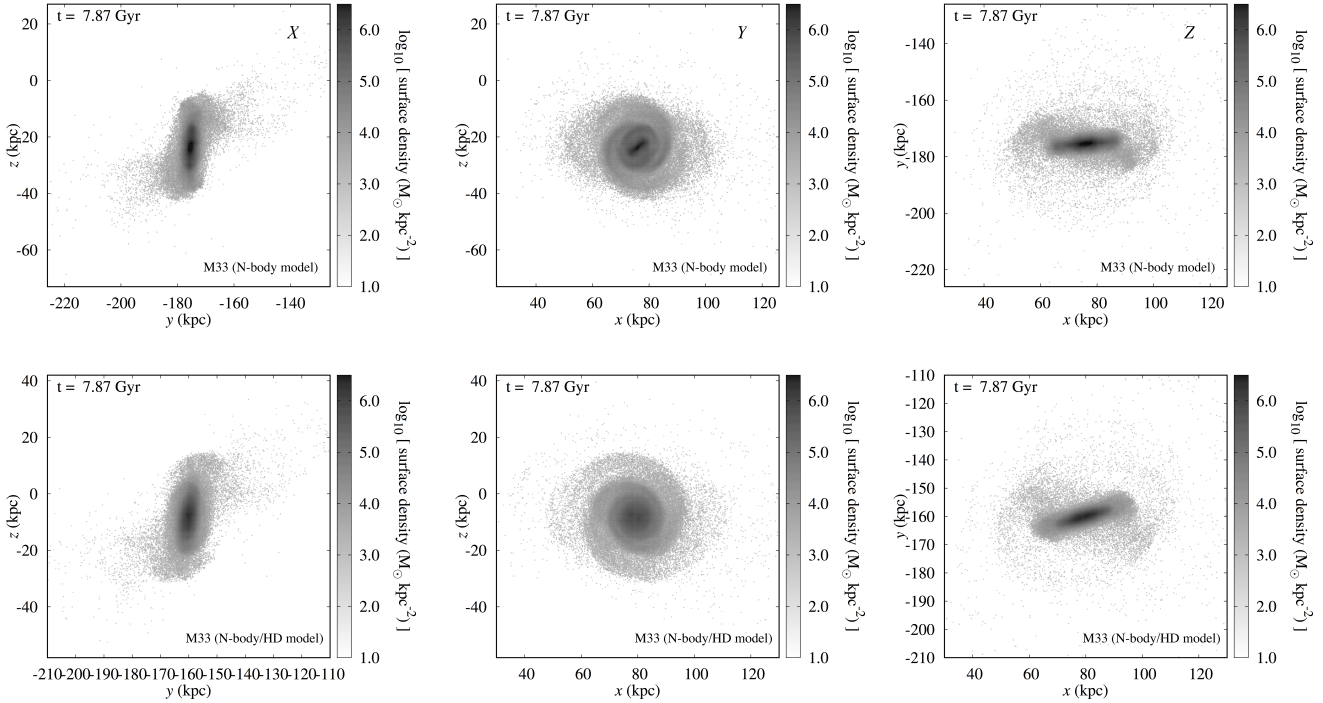


**Figure 4.** Simulated distribution of stars in M33 at the present epoch, i.e.  $\sim 7$  Gyr after M33 first crossed M31’s virial radius, and  $\sim 6.5$  Gyr since their closest encounter. From left to right, each panel displays the surface density of stars associated to M33 projected along the  $x$ -,  $y$ -, and  $z$ -axis, respectively. Top: N-body model. Bottom: Full N-body/hydrodynamical model. Note the presence of a bar in the pure N-body model. Note that the coordinate frame has its origin at the initial position of M31.

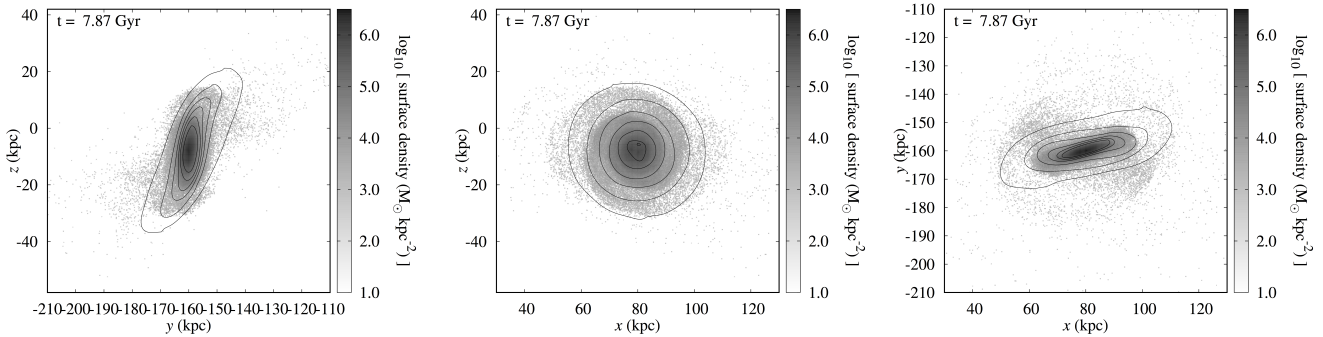


**Figure 5.** Same as the stellar distribution displayed in the bottom row in Fig. 4, but with total gas column density contours overlaid. The contour levels indicate, starting from the innermost, a total gas column density  $\log[N_{\text{gas}}/\text{cm}^{-2}] = 21.4 - 19.4$  in steps of 0.4 dex. The warp of the gas disc is apparent. Note that the coordinate frame has its origin at the initial position of M31.

obtained from the use of pure semi-analytic methods. This implies the need to revisit previous studies about the orbital histories of galaxy pairs that have ignored dynamical mass loss and the use of N-body simulations.

That said, it is important to emphasize that the two diametrically different orbital solutions, i.e. a first-infall and one featuring a close encounter in the distant past (‘second infall’) are in fact possible. A first-infall solution is consistent with an insignificant dynamical mass loss. In contrast, a second-infall solution as the one we have found requires M33 to have lost roughly half its mass to tidal stripping as a result of the close encounter. In other words, a preference for either orbit family can only be expressed if the

mass evolution of M33 was known. In particular, it is necessary to constrain both M33’s present-day mass and its infall mass.

In spite of the plausibility of the two different solutions, there is a wealth of evidence firmly supporting the belief that M33 had a strong tidal interaction with M31 in the past. These include the disturbed stellar morphology of M33 and its warped gas disc, and the H $\alpha$  filament between these two galaxies. Stated somewhat differently, the disturbed morphology of the stellar distribution and the gas distribution of M33, and the presence of the M31-M33 H $\alpha$  filament, are the most puzzling properties of the Andromeda system in the framework of a first-infall scenario (for a discussion see Patel et al. 2017). Indeed, with no obvious perturber other than M31, it is hard to understand how M33’s disturbed structure came about to be.

The idea that the H<sub>1</sub> filament may result from the condensation of IGM gas, while not unreasonable, may require very special conditions (Binney et al. 2009). If the condensation is happening along a DM filament spanning between these two galaxies as suggested by some (e.g. Braun & Thilker 2004), then the origin of this structure needs to be explained. In contrast, a close encounter between these galaxies may naturally explain all of these observations – at least qualitatively – as others have argued before us (albeit using different orbital constraints, e.g. McConnachie et al. 2009, and less sophisticated models, e.g. Bekki 2008).

Our model featuring a close encounter in the remote past cannot reproduce M31’s Giant Stellar Stream. This is consistent with the idea that the Giant Stellar Stream is a young feature (< 1 Gyr) induced by the direct collision of M31 with a satellite with a possible range of masses ( $\sim 10^9 - 10^{11} M_{\odot}$ ) (Fardal et al. 2006; Hammer et al. 2018). Therefore, the observation of the stellar stream and the reality of a close encounter between M31 and M33 in the distant past are not mutually exclusive. Finally, the epoch of the pericentric passage suggested by our orbital solution ( $\sim 6.5$  Gyr ago) corresponds to a redshift  $z \approx 0.75$  in a 737-cosmology, i.e.  $(h, \Omega_b, \Omega_{\Lambda}) = (0.7, 0.3, 0.7)$ . This epoch is consistent with the age of the dominant stellar population in the outer radii of M33 (Williams et al. 2009), suggesting that these stars may have formed as a result of an increased star formation likely triggered by the close encounter between these galaxies (e.g. Mayer et al. 2001).

Based on the above discussion we are strongly inclined to believe that M31 and M33 truly had a close encounter in the past.

A corollary of our model is the putative existence of a gas stream, the ‘Triangulum stream’, trailing M33. This stream has not yet been observed, although a possibly associated, high-density structure may already be discernible in the H<sub>1</sub> maps of M33 presented by Putman et al. (2009). We can think of a number of reasons why, if existent, this stream has not been detected yet. Our model suggests that the stream is very diffuse with a *total* gas column density of  $\sim 10^{18} \text{ cm}^{-3}$ . In addition, the gas along the stream could be highly ionized. And its distribution could be clumpy (Bland-Hawthorn et al. 2017). Therefore, the stream may have a neutral fraction that is too low to be observable with current radio facilities as a result of their limited sensitivity.

Largely dependent upon ionization fraction, deep observations with FAST, such as the GAS survey, could potentially reach the required sensitivity to look for the presence of the Triangulum stream. It is worth noting that not even SKA1 will be as sensitive to extended HI emission in the Local Volume. Other potential probes include targeting QSOs behind the region around M33, imaging H $\alpha$  around M33, and X-ray spectroscopy. So far, there are no H $\alpha$  observations beyond the optical disc (e.g. Kam et al. 2015, see also Zheng et al. 2017), and observations targeting a wider field would be required.

We conclude by highlighting some potential shortcoming of our model, and suggesting avenues for improvement. Firstly, we did not explore the role different initial relative inclination of the galaxies play in the final configuration of the system. M33 is observed to lie roughly along the minor axis of M31 (see Lehner et al. 2015, their figure 1). This configuration is not faithfully reproduced by our models. However, it should not be difficult to come up with an initial relative orientation that agrees with the observed one. Secondly, we did not explore variations in the mass models of the galaxies, i.e. their total masses and its distribution. But the total mass we have adopted for each galaxy is each consistent with a range of observations, and consistent with the masses adopted in earlier studies. Still,

it should prove useful to explore different mass ranges as well as different mass profiles. Thirdly, the IGM in our full simulation may be too diffuse compared to the Local Group IGM. In consequence, we may have likely underestimated the ram pressure exerted by the intra-group medium onto the gas streams which results from the motion of the system’s barycentre through the IGM. Finally, we did not perform a test for the convergence of our simulation results. However, in Tepper-García et al. (2019) we demonstrated that the limiting resolution we have adopted here is enough to model the global structure of gas streams around galaxies. Nonetheless, in order to properly model the small-scale distribution of gas in the streams may require a higher resolution. With exception of the mass models, we expect all of the above to have an effect only on the *detailed* structure of the tidal debris, but not the large-scale features. These model improvements, in addition to a statistical analysis of the possible orbit families, and detailed ionization calculations are left for future work.

## ACKNOWLEDGMENTS

This work is partially supported by the National Natural Science Foundation of China grant No. 11988101. TTG acknowledges financial support from the Australian Research Council (ARC) through an Australian Laureate Fellowship awarded to JBH. We acknowledge the facilities, and the scientific and technical assistance of the Sydney Informatics Hub (SIH) at the University of Sydney and, in particular, access to the high-performance computing facility Artemis and additional resources on the National Computational Infrastructure (NCI), which is supported by the Australian Government, through the University of Sydney’s Grand Challenge Program the *Astrophysics Grand Challenge: From Large to Small* (CIs: Geraint F. Lewis and JBH). We made use of pynbody<sup>13</sup> in our analysis for this paper. All figures and movie frames created with GNUPLOT, originally written by Thomas Williams and Colin Kelley.<sup>14</sup> All animations assembled with FFmpeg.<sup>15</sup> This research has made use of NASA’s Astrophysics Data System (ADS) Bibliographic Services<sup>16</sup>, and of ASTROPY,<sup>17</sup> a community-developed core PYTHON<sup>18</sup> package for Astronomy (Astropy Collaboration 2013).

## References

- Astropy Collaboration et al., 2013, *A&A*, 558, A33
- Bekki K., 2008, *MNRAS*, 390, L24
- Bernard E. J., Ferguson A. M. N., Chapman S. C., Ibata R. A., Irwin M. J., Lewis G. F., McConnachie A. W., 2015, *MNRAS*, 453, L113
- Binney J., Nipoti C., Fraternali F., 2009, *MNRAS*, 397, 1804
- Bland-Hawthorn J., Gerhard O., 2016, *Annual Review of Astronomy and Astrophysics*, 54, 529
- Bland-Hawthorn J., Maloney P., Stephens A., Zovaro A., Popping A., 2017, preprint, ([arXiv:1709.08733](https://arxiv.org/abs/1709.08733))
- Braun R., Thilker D. A., 2004, *A&A*, 417, 421

<sup>13</sup> <https://github.com/pynbody/pynbody>

<sup>14</sup> <http://www.gnuplot.info>

<sup>15</sup> <http://www.ffmpeg.org>

<sup>16</sup> <http://adsabs.harvard.edu>

<sup>17</sup> <http://www.astropy.org>

<sup>18</sup> <http://www.python.org>

Corbelli E., Thilker D., Zibetti S., Giovanardi C., Salucci P., 2014, *A&A*, **572**, A23

Courteau S., Widrow L. M., McDonald M., Guhathakurta P., Gilbert K. M., Zhu Y., Beaton R. L., Majewski S. R., 2011, *ApJ*, **739**, 20

Dalcanton J. J., et al., 2012, *ApJS*, **200**, 18

Diaz J. D., Koposov S. E., Irwin M., Belokurov V., Evans N. W., 2014, *MNRAS*, **443**, 1688

Dierickx M. I. P., Loeb A., 2017, *ApJ*, **836**, 92

Dorman C. E., et al., 2015, *ApJ*, **803**, 24

Fardal M. A., Babul A., Geehan J. J., Guhathakurta P., 2006, *MNRAS*, **366**, 1012

Fardal M. A., et al., 2013, *MNRAS*, **434**, 2779

Ferguson A. M. N., Mackey A. D., 2016, Substructure and Tidal Streams in the Andromeda Galaxy and its Satellites. Springer, p. 191, doi:10.1007/978-3-319-19336-6\_8

Gilbert K. M., et al., 2009, *ApJ*, **705**, 1275

Hammer F., Yang Y. B., Wang J. L., Ibata R., Flores H., Puech M., 2018, *MNRAS*, **475**, 2754

Hashimoto Y., Funato Y., Makino J., 2003, *ApJ*, **582**, 196

Hernquist L., 1990, *ApJ*, **356**, 359

Hou J. L., Prantzos N., Boissier S., 2000, *A&A*, **362**, 921

Ibata R., Irwin M., Lewis G., Ferguson A. M. N., Tanvir N., 2001, *Nature*, **412**, 49

Ibata R. A., et al., 2014, *ApJ*, **780**, 128

Jiang I.-G., Binney J., 2000, *MNRAS*, **314**, 468

Kalberla P. M. W., Kerp J., 2009, *ARA&A*, **47**, 27

Kam Z. S., Carignan C., Chemin L., Amram P., Epinat B., 2015, *MNRAS*, **449**, 4048

Kam S. Z., Carignan C., Chemin L., Foster T., Elson E., Jarrett T. H., 2017, *AJ*, **154**, 41

Kerp J., Kalberla P. M. W., Ben Bekhti N., Flöer L., Lenz D., Winkel B., 2016, *A&A*, **589**, A120

Klypin A., Gottlöber S., Kravtsov A. V., Khokhlov A. M., 1999, *ApJ*, **516**, 530

Koch A., Danforth C. W., Rich R. M., Ibata R., Keeney B. A., 2015, *ApJ*, **807**, 153

Kormendy J., 2013, Secular Evolution in Disk Galaxies. Cambridge University Press, p. 1

Kourkchi E., Tully R. B., 2017, *ApJ*, **843**, 16

Lehner N., Howk J. C., Wakker B. P., 2015, *ApJ*, **804**, 79

Lewis G. F., et al., 2013, *ApJ*, **763**, 4

Li D., Pan Z., 2016, *Radio Science*, **51**, 1060

Li D., et al., 2018, *IEEE Microwave Magazine*, **19**, 112

Lockman F. J., Free N. L., Shields J. C., 2012, *AJ*, **144**, 52

Mayer L., Governato F., Colpi M., Moore B., Quinn T., Wadsley J., Stadel J., Lake G., 2001, *ApJ*, **547**, L123

McConnachie A. W., et al., 2009, *Nature*, **461**, 66

McConnachie A. W., et al., 2018, *ApJ*, **868**, 55

McMillan P. J., 2017, *MNRAS*, **465**, 76

Miller M. J., Bregman J. N., 2015, *ApJ*, **800**, 14

Mould J., 2013, *PASA*, **30**, e027

Nan R., et al., 2011, *International Journal of Modern Physics D*, **20**, 989

Navarro J. F., Frenk C. S., White S. D. M., 1997, *ApJ*, **490**, 493

Nichols M., Bland-Hawthorn J., 2009, *ApJ*, **707**, 1642

Patel E., Besla G., Sohn S. T., 2017, *MNRAS*, **464**, 3825

Perret V., Renaud F., Epinat B., Amram P., Bournaud F., Contini T., Teyssier R., Lambert J.-C., 2014, *A&A*, **562**, A1

Plummer H. C., 1911, *MNRAS*, **71**, 460

Putman M. E., et al., 2009, *ApJ*, **703**, 1486

Salomon J.-B., Ibata R. A., Famaey B., Martin N. F., Lewis G. F., 2016, *MNRAS*, **456**, 4432

Sellwood J. A., Shen J., Li Z., 2019, *MNRAS*, **486**, 4710

Semczuk M., Łokas E. L., Salomon J.-B., Athanassoula E., D'Onghia E., 2018, *ApJ*, **864**, 34

Tanaka M., Chiba M., Komiyama Y., Guhathakurta P., Kalirai J. S., Iye M., 2010, *ApJ*, **708**, 1168

Tenjes P., Tuvikene T., Tamm A., Kipper R., Tempel E., 2017, *A&A*, **600**, A34

This paper has been typeset from a *TeX/LaTeX* file prepared by the author.